Precision magnetic field mapping for CERN experiment NA62

2016 J. Phys. G: Nucl. Part. Phys. 43 125004

(http://iopscience.iop.org/0954-3899/43/12/125004)

OPEN ACCESS
IOP Publishing
Journal of Physics G: Nuclear and Particle Physics
J. Phys. G: Nucl. Part. Phys. **43** (2016) 125004 (19pp)
doi:10.1088/0954-3899/43/12/125004

Precision magnetic field mapping for CERN experiment NA62

John R Fry[1,3], Giuseppe Ruggiero[1,2] and Felix Bergsma[2]

[1] Department of Physics, University of Liverpool, Liverpool L69 7ZE, UK
[2] EP Department, CERN, Geneva 23, Switzerland

E-mail: JRF@Liverpool.ac.uk

Received 21 July 2016, revised 3 September 2016
Accepted for publication 29 September 2016
Published 16 November 2016

Abstract

In the CERN experiment NA62, low-mass straw-tube tracking-chambers have been designed to operate in vacuum and, in conjunction with precisely mapped magnetic fields, enable the determination of the trajectories of the charged decay products of a 75 GeV/c K^+ with high accuracy. This is particularly important for the crucial measurement of the branching fraction for the decay $K^+ \rightarrow \pi^+ \nu \nu$, which has the potential to reveal BSM physics. The charged particles passing through the magnetic field of a dipole magnet receive a transverse-momentum kick, $\Delta P_T = 270$ MeV/c, which the physics requires to be determined to better than one part in a thousand. This puts stringent constraints on the required accuracy and precision of the magnetic field components at all points through which charged particles pass. Before reaching the dipole magnet the particles travel through an evacuated steel tank of length 90 m, where residual magnetic fields of typical size 50 μT modify the trajectories of the charged particles and require measurement with a precision of better than 10 μT. In this paper we describe in detail the different approaches to the measurement and analysis of the magnetic field for the two regions, the corrections to the raw data necessary to produce the final field map, and the physics validation procedures showing that the required accuracy and precision of the field maps have been achieved.

Keywords: CERN, NA62, precision measurement, magnetic field

(Some figures may appear in colour only in the online journal)

[3] Author to whom any correspondence should be addressed.

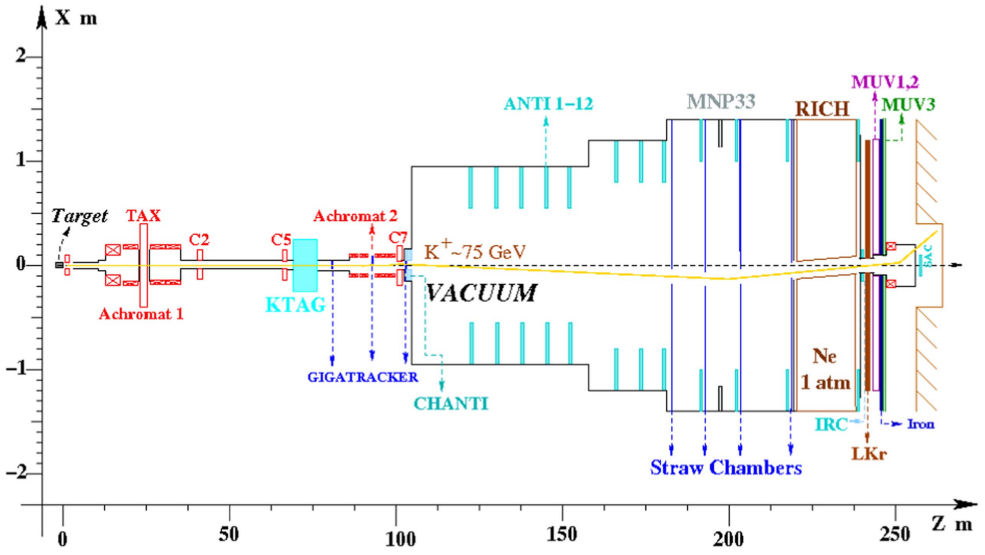

Figure 1. The layout of detectors in the NA62 experiment as viewed from above. The coordinate system is right-handed with its origin at the target; the Z axis is along the beam direction and Y vertically up (out of the page). The dipole magnet MNP33 is situated at $Z = 197$ m and its aperture extends 1.3 m in Z and ± 1 m in both X and Y.

1. Introduction

CERN experiment NA62 has been designed to study ultra-rare decays of the charged kaon with a view to observing effects different from those predicted by the Standard Model (SM) and thereby opening a window onto new physics complementary to the direct searches of LHC. The flagship decay, $K^+ \to \pi^+ \nu\,\nu$, is predicted by the SM [1] to occur with a branching fraction (BF) of less than 10^{-10} with a theoretical uncertainty of less than 10%, and a deviation from this value would be *prima facia* evidence for new physics beyond the SM. Over the 3 year period of data-taking, starting in 2016, a beam flux of 10^{13} K^+ is expected to produce more than 100 such decays [2] enabling a measurement of the BF to better than 10%. Charged kaons form 6% of the high-intensity (750 MHz) unseparated charged-particle beam of momentum 75 GeV/c and are tagged with a time-stamp of better than 100 ps using a differential, ring-focussing Cherenkov counter (KTAG); the position and momentum vector of each K^+ is then measured with high precision using a beam spectrometer formed from three stations of silicon-pixel, Giga-tracker detectors (GTK) and a magnetic achromat, prior to an evacuated decay region of 90 m, as shown in figure 1. The momenta of charged secondary particles lie within the range 10–60 GeV/c, while the momentum of the π^+ in the flagship decay is required to be within 15–35 GeV/c to ensure that the dominant background decays have a large neutral energy.

The precise time resolution of $<$200 ps achieved by GTK enables much of the background due to overlapping beam tracks to be removed, while KTAG reduces background from non-decaying beam particles that interact with the residual gas molecules. The spatial coordinates and momenta of the charged decay products of the K^+ are measured using two pairs of low-mass straw chambers operating in vacuum (STRAW), one pair on either side of dipole magnet MNP33, and their identity determined using a ring-imaging Cherenkov counter (RICH) together with hadron calorimeters and muon chambers (MUV). The time resolution

(100 ps) of the RICH in conjunction with that of KTAG ensures that secondary particles are associated with the tagged K^+. Photons are detected, and their energies and timestamps measured, using a hermetic array of lead-glass blocks (LAV) situated in 12 stations along the beamline together with a highly-segmented liquid-Krypton calorimeter (LKR) placed between RICH and MUV; small-angle calorimeters IRC and SAC complete the angular coverage. A fuller and more systematic description of the operating NA62 detector is in preparation, but all essential details may be found in the NA62 Technical Design Report [3].

The major challenge in the experiment is to reduce the enormous background to the wanted signals. This is done using two complementary approaches. To a large extent background decays are rejected by identifying the measured energy deposits using photon, hadron and muon calorimetry together with the RICH Cherenkov detector, and in a complementary manner kinematic constraints enable a further large reduction in unwanted decay modes. A key quantity in the kinematic rejection of unwanted decays is the measurement of the missing-mass squared, the square of the difference in kaon and pion momentum four-vectors, $M_{\mathrm{miss}}{}^2 = (P_{\mathrm{K}}{}^+ - P_{\pi}{}^+)^2$, where separation between signal and background depends critically on having excellent resolution. The precision on $M_{\mathrm{miss}}{}^2$ will be spoiled if the particle momenta are badly measured, and hence the precise determination of the transverse-momentum kick, ΔP_{T}, given to each charged particle is essential so that the deflection of the trajectory between the pairs of straw chambers on either side of the dipole magnet can be converted into an accurate measurement of momentum. The precision on the measurement of ΔP_{T} corresponds to that on the field integral, $\int \mathbf{B}.\mathrm{d}\mathbf{L}$, for the particular trajectory through the magnet and hence requires the precise determination of an accurate three-dimensional magnetic-field map for the dipole magnet and its fringe field.

Since mapping the magnetic fields for NA48/2 [5] the dipole magnet and evacuated tubes have been substantially rebuilt and hence a complete re-mapping of both fields over a combined volume of more than 600 m^3 was essential. The physics requirement for NA62 is for ΔP_{T}, and hence $\int \mathbf{B}.\mathrm{d}\mathbf{L}$, to be determined to better than one part in a thousand in order to preserve the precision on the angles of particles measured by the tracking system. To set the scale for the magnetic-field measurements of the dipole magnet MNP33: $\int B_Y \,\mathrm{d}Z = 0.90$ T m, corresponding to a momentum kick on each charged secondary particle of $\Delta p_{\mathrm{T}} = 270$ MeV/c, while the major component of the magnetic field, B_Y, in the centre of the magnet is approximately 0.4 T. This translates to a maximum permitted systematic uncertainty on the field integral of $\Delta \int B_Y \,\mathrm{d}Z < 10^{-3}$ T m. The physics is insensitive to the z component of magnetic field, since the secondary charged tracks are rather parallel to the z axis with an angle <20 mrad, and furthermore B_Z is anti-symmetric about the centre of the magnet. Thus, the systematic uncertainties on both B_X and B_Y are required to be smaller than 2×10^{-4} T throughout the effective magnetic volume of the dipole.

Before reaching the dipole magnet the charged particles travel through an evacuated steel tank of length 90 m, where the K^+ is required to decay, and residual magnetic fields of typical size 50 μT modify the trajectories of the particles. From previous measurements of the magnetic field in the evacuated region as it was configured for NA48/2, the progenitor of NA62, a charged particle of 25 GeV/c was deflected by 35 μrad, which corresponds to $\int \mathbf{B}.\mathrm{d}\mathbf{L} = 3 \times 10^{-3}$ T m and a momentum kick of $\Delta p_{\mathrm{T}} = 0.9$ MeV/c. This gave rise to an uncertainty of 1.5×10^{-3} (GeV/c^2)^2 in the computation of the missing mass squared to the π^0 in the decay $K^+ \to \pi^+ \pi^0$ and an azimuthal asymmetry of ± 0.5 MeV/c^2 (about 30% of the resolution) in the invariant mass of the three pions in the decay $K^+ \to \pi^+ \pi^+ \pi^-$ [4]. After incorporation of the residual-field map into the analysis software, the resulting azimuthal asymmetry in the 3π invariant mass was reduced to ± 50 keV/c^2, corresponding to an uncertainty of 4×10^{-4} T m in $\int \mathbf{B}.\mathrm{d}\mathbf{L}$. The aim for NA62 is to ensure that the combined

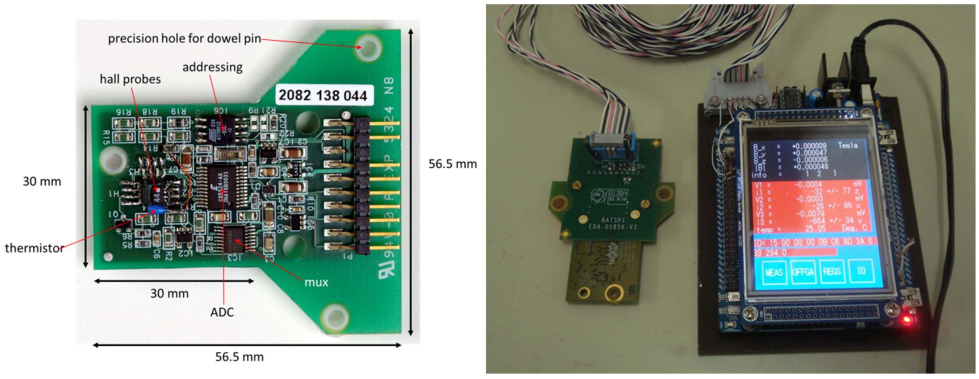

Figure 2. Circuit board comprising three orthogonal Hall probes (left); readout monitor (right).

uncertainty on the integrated residual field measurements in the evacuated tubes and the fringe field of the dipole magnet is small compared with that for MNP33. We therefore require $\Delta\int\mathbf{B}.\mathrm{d}\mathbf{L} < 3 \times 10^{-4}$ T m for these contributions which, from a comparison with NA48/2, will give negligible disturbance to the measurement of kinematical variables in all of the decay modes of the charged kaon.

The design goals for the three-dimensional magnetic field map are such that the fundamental precision of the tracking system is never compromised. The uncertainties on both components of the integrated magnetic field $[\int B.\mathrm{d}z]$ along the beam direction over the complete kaon decay region, or any smaller region in which the kaon may decay, are smaller than 3×10^{-4} T m. This integrated field corresponds to a transverse momentum uncertainty of 0.1 MeV/c, which would give rise to an angular uncertainty of <2 μrad in the angle of the kaon to be compared with the measurement uncertainty of 20 μrad for the GTK system. The magnetic field has no detectable effect on the magnitude of the kaon momentum, while the GTK system measures the momentum of the kaon to 0.2%. The deflection of a charged particle of momentum 10–60 GeV/c passing through the magnetic field of the dipole varies from 27 to 4.5 mrad, with an uncertainty of better than one part in a thousand on both angle and momentum from knowledge of the integrated magnetic field. By design the STRAW chambers measure the deflection of a charged particle to 60 μrad, while the momentum is typically measured to 1%, dominated at lower momenta by multiple Coulomb scattering.

2. Magnetic-field measurements

To ensure complete coverage of the kaon-decay particles required for physics, magnetic-field measurements within the evacuated region were made covering a cone of half-angle 20 mrad subtended at the GTK-3 plane and extending into the fringe field of MNP33 beyond the STRAW-2 detector, a total distance of 90 m. The magnetic field of dipole magnet MNP33 was measured over a grid spanning ± 4 m along the beam axis (Z direction) about the centre of the magnet and over the entire aperture of the magnet in the transverse X–Y plane. The fringe-field region is defined empirically to be the region within the evacuated tubes extending from the small, rather constant values of B_X and B_Y to just beyond the commencement of measurements of the dipole field 4 m from its centre, and stretched

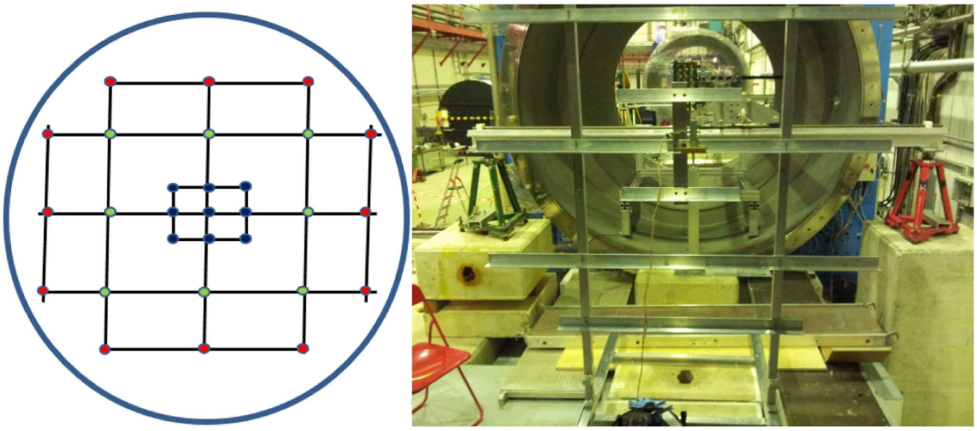

Figure 3. Measurement grid showing all 29 coordinates (left); measurement structure in the fringe-field region allowing all 29 coordinate measurements, with Hall-probe sensor at centre (right).

(approximately) from $Z = 185$ to 193 m. The two independent sets of measurements of the fringe field, one made in the evacuated region while the other was made on the MNP33 grid, overlapped to enable a check on consistency and systematic errors.

The Hall-probe sensor used throughout this work comprised three orthogonal Hall probes of type Siemens KSY44 to measure the X, Y and Z-components of the magnetic field at a given position. They were mounted on a circuit board, with electronics providing temperature-corrected calibration and offsets, as shown in figure 2, lhs. High-field [0–1.4 T] calibration was performed using a rotative calibrator, while low-field [0–4 mT] calibration was done using a Helmholtz coil. As part of the calibration procedure measured parameters ensured orthogonality of the field components with an accuracy of mrad. Reconstruction of the field was performed using an ARM CORTEX processor using the many stored parameters to model the temperature and magnetic-field calibrations. For the measurements of magnetic field in the evacuated tubes the sensor card was linked to a monitor (figure 2, rhs) displaying all three components of field.

2.1. Measurement of the magnetic fields in the evacuated tubes

For these measurements the Hall-probe sensor was connected to a rigid frame that allows stable and reproducible positioning, together with rotation about two axes, to achieve any desired directional orientation. It was designed to measure magnetic fields of the order of 1 T in the ATLAS experiment [6] with offsets reproducible to about 50 μT. However, the residual magnetic fields in the NA62 evacuated tubes vary within the range $10-100$ μT and a modification to the software was therefore made to take the average of many repeated calibrations, which resulted in stable offsets that were reproducible to better than 10 μT.

Measurements of the magnetic-field components along three orthogonal axes were made over a grid in the X–Y plane at particular values of Z. The measurements were typically made every 2–3 m over the 100 m distance from GTK_3 to MNP33, although the spacing was 1 m nearest to GTK-3 where B_X varied particularly rapidly; this also simplified the calculation of a bound on the sampling error resulting from having a finite step size, rather than continuous values of Z. The magnitude of the fringe field of MNP33 varies rapidly over a relatively short distance, and it was measured at intervals of 0.3 m in Z in

Figure 4. Sensor panel comprising 10 × 3 Hall-probe cards (left); measurement rails and chassis (right).

order accurately to map its behaviour. Over approximately the first 15 m downstream of GTK-3 a central point and eight additional points, equally spaced around a square of side length 40 cm in the *X*–*Y* plane, covered the decay volume. Over the next 35 m an additional 8 points were measured, equally spaced around a square of side length 100 cm. Finally, over the last 50 m an additional 12 points were measured, spaced around a square of side length 160 cm, to give a total of 29 measurements in the *X*–*Y* plane at each *Z* position, as shown in figure 3.

Repeated measurements of the magnetic-field components were made to ensure reproducibility to better than 10 μT, while consistency in the measurement of offsets before and after the magnetic-field measurements was also required to be better than 10 μT. Offsets contribute the same systematic error to every measurement of magnetic field within each plane and hence the uncertainties are added linearly. By measuring the offsets for each plane separately, however, the individual measurements for each plane at a given value of *Z* are uncorrelated with those of any other plane at a different value of *Z*, and the resulting uncertainties from the different planes may be combined in quadrature when calculating their contribution to the error in $\int \mathbf{B}.\mathrm{d}\mathbf{L}$.

2.2. Measurement of the magnetic field in the MNP33 dipole magnet

The dipole magnet MNP33 has transverse dimensions of 2.3 m × 2.3 m and is of length 1.2 m. The (circular) beam pipe is of diameter 2 m and fits inside the magnet aperture. Because of instrumental limitations the magnetic field of MNP33 was mapped in two halves, each covering the entire *X*–*Y* plane over 4 m in *Z*, with one half upstream and the other downstream of the centre of the magnet; there was a small overlap region at the centre to enable consistency checks to be made between the two sets of measurements. The measurement frame consisted of two panels, each holding 30 identical sensor cards (figure 4, left) comprising three mutually-perpendicular Hall probes in a 10 × 3 array on a grid of spacing 80 mm in both *X* and *Y*. The high-field calibration enabled a measurement precision of 0.2 mT. The Hall probes on the front and back panels all faced outwards, so that the relative signs of two of the magnetic-field components were reversed from front to back panel by a rotation about the panel axis. The two panels, separated by 63.8 mm in *Z*, were firmly attached to a pair of rails fixed to a chassis (figure 4, right) and could be driven under computer control in the $\pm Z$ direction with a precision of 0.1 mm. Measurements of the three components of magnetic

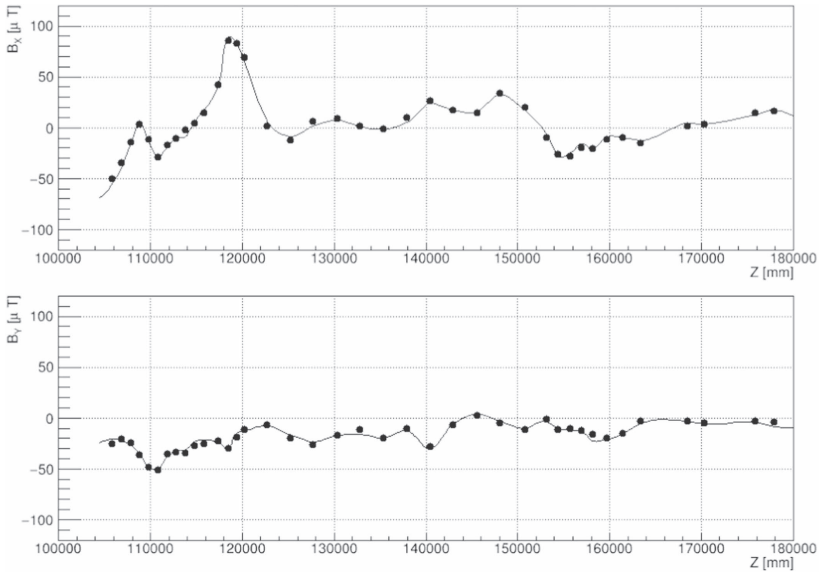

Figure 5. Variation of B_X (top) and B_Y (bottom) with Z at the beam position over the K^+ decay region. The points show experimental measurements while the curves are the empirical interpolation of the data.

field were read out for all 60 Hall probes at any desired spacing in Z. The bulk of the measurements from which the final field map was produced were taken with a spacing of 80 mm in Z, so that a given data set comprised approximately 3000 measurements of each of the three magnetic-field components.

The rails were displaced vertically or horizontally in fixed steps of 80 mm to enable 'up' measurements to cover the upper half of the magnet aperture for values of $Y \geqslant 360$ mm and all available values of X. It was desirable to achieve significant overlap in the positions of the panels to enable comparison of the magnetic-field measurements made by different Hall probes at the same point in space and a total of 14 such data sets was recorded. To measure the magnetic field in the lower portion, 'down', of the X–Y aperture, the rails, to which the panels were rigidly fixed, were unbolted from the chassis and rotated through 180°. A similar set of 14 data sets was recorded for values of $Y \leqslant -360$ mm and all available values of X. Measurements within the central region of the magnet aperture, that is for $-360 \leqslant Y \leqslant +360$ mm, were made by rotating the rails by $\pm 90°$; 12 such 'Rot ± 90' data sets were recorded, making a total of 40 data sets for upstream data. To enable downstream data to be recorded, the entire chassis was removed and re-installed downstream of the centre of the magnet, giving a grand total of 80 data sets each comprising 3000 measurements. In addition, a special data set was recorded with zero magnetic field, and another with the Hall probes having the same orientation on the back and front panels—this latter being achieved by unbolting the back panel and screwing it back onto the rails in the reverse orientation. The various rotations of the panels about the Y and Z axes mean that a particular Hall probe may measure a different component of the magnetic field in the different data sets.

3. Analysis of the magnetic-field data for the K^+ decay volume and MNP33 fringe field

3.1. Behaviour of the magnetic field

The behaviour of B_X and B_Y along the beamline is shown by the solid points in figure 5. The vertical component, B_Y, is negative and <20 μT a.e., while the horizontal component, B_X, rises to almost 100 μT downstream of the third Giga-Tracker station and then changes sign. The magnetic-field distributions are complex since the 'residual' field is strongly affected by the presence of flanges and man-hole covers along the evacuated tubes, where the magnetic domains have re-arranged themselves under the stress of work-hardening. The integrated magnetic field components along the beamline over the K^+ decay region, $105 < Z < 180$ m, have values of $\int B_X \, dZ = 375$ μT m and $\int B_Y \, dZ = -1160$ μT m and show excellent consistency over the central region, with a variation of $<5\%$. Although the magnetic-field components are everywhere comparable with the Earth's magnetic field of ≈ 30 μT, the measured values of integrated magnetic field indicate that the evacuated tubes give a net screening effect.

Downstream of the decay region, where STRAW chambers 1 and 2 are situated, the effects of the fringe field of dipole magnet MNP33 become increasingly large, with the dominant component, B_Y, increasing to $\sim$5 mT at 4 m from the centre of the magnet. As expected, values of B_X in the central region of the X–Y plane are everywhere small (<100 μT), while at large values of X and Y, B_X increases in magnitude to $\sim$0.2 mT as the dipole magnet is approached, and reverses sign with Y. For the fringe-field region, $185 < Z < 193$ m, the values of integrated field for the X and Y components are 215 μT m and 5390 μT m, respectively. From the symmetry of the dipole field an equal contribution arises from the downstream fringe field between $Z = 201$ and 209 m. Thus, the Y-component of the fringe field contributes approximately 1.2% of the total p_T kick given to charged particles.

3.2. Field map for the decay region comprising the evacuated tubes

Whereas the measured magnetic-field components span a grid of finite spatial intervals within the K^+ decay phase space, physics requires knowledge of the magnetic field at all intermediate points in space. This is obtained by interpolating the measured values in X, Y and Z using simple polynomials, and the computer code for doing this has been incorporated into the NA62 software package. The curves in figure 5 show the interpolated predictions to the data and agreement with the measured field integrals is good to 10–20 μT m everywhere that direct checks can be made. The authors have validated their interpolation using the MC simulated decays $K^+ \to \mu^+ \nu$ and $K^+ \to \pi^+ \pi^+ \pi^-$, where in the latter case disregarding the magnetic field in the evacuated decay region gave rise to an azimuthal asymmetry of ± 0.25 MeV/c^2 in the invariant mass, which was removed when using the precise measurement of the field integrals—see figure 12(b) and the discussion in section 5.

3.3. Evaluation of the uncertainties, $\Delta\int B_X \, dZ$ and $\Delta\int B_Y \, dZ$, for the decay and fringe-field regions

For each X, Y coordinate at a fixed value of Z within the decay volume, the magnetic-field components were measured several times. The resulting statistical uncertainty was added linearly to the offset error, which applied to all measurements on the transverse plane at a particular value of Z, to give the overall measurement error for the coordinate X, Y, Z. Since all measurements on transverse planes at different values of Z are independent, these

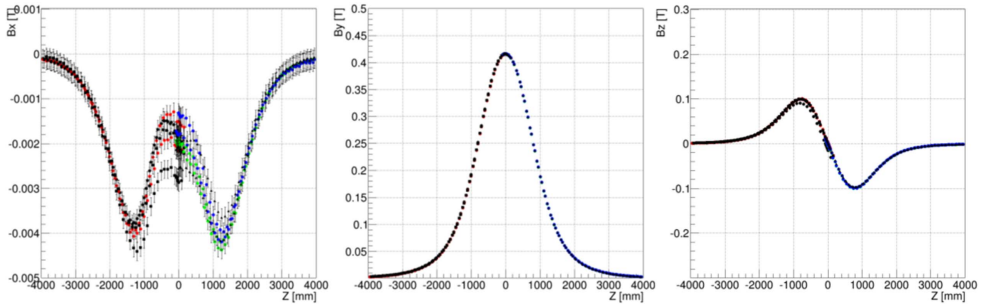

Figure 6. Plotted at $X = 40$, $Y = 360$ mm are: (left) B_X versus Z, (centre) B_Y versus Z and (right) B_Z versus Z. The different colours and symbols are used to enable points from different sensors to be distinguished.

measurement errors were added in quadrature to give the resultant measurement uncertainties on the values of integrated field for a particular value of X and Y. These uncertainties were calculated to be 90 μT m for both $\int B_X \, dZ$ and $\int B_Y \, dZ$. Sampling errors, arising from the discrete values of Z at which field measurements were made, gave rise to uncertainties of 80 and 30 μT m, respectively in the integral X and Y magnetic fields. Uncertainties arising from wrongly positioning the Hall-probe sensor in X, Y and Z were investigated but found to be negligible. The combined systematic uncertainties for the integral X and Y magnetic-field components for the K^+ decay volume are 120 μT m and 100 μT m respectively.

The largest systematic uncertainty, 50 μT m, for the fringe field arises because of the mixing of the relatively large vertical component of the field, B_Y, into the smaller horizontal component, B_X, due to possible angular misalignment of the Hall-probe sensor. The contributions from measurement and sampling uncertainties were 17 and 10 μT m, respectively, for the X and Y field-integral component. Doubling these errors to take into account the unmeasured downstream field integrals gives total contributions of 120 and 40 μT m for the X and Y components.

Combining the errors from the decay and fringe-field regions gives 170 and 110 μT m for the X and Y components of the field integrals, respectively, which comfortably meet the requirement outlined in the introduction, namely that $\Delta \int \mathbf{B}.d\mathbf{L} < 3 \times 10^{-4}$ T m.

4. Analysis of the magnetic-field data for the MNP33 dipole magnet

Because of the particular symmetry properties of the magnetic-field components of a dipole magnet the analysis in this section is greatly simplified by referring all Z coordinates to an origin at the centre of magnet MNP33. The range in Z is then ± 4 m.

At the heart of each sensor card are three Hall probes glued to the sides of a cube of side 4 mm to provide measurements of the three orthogonal components of the magnetic field at locations in space that are very close to each other. The orientation of the sensor cards is such that each of the three Hall-probe measurements, referred to as B_1, B_2, and B_3, corresponds to one of the magnetic field components in the NA62 coordinate system, referred to as B_X, B_Y, and B_Z. Depending on the orientation of the sensor card, however, the correspondence varies. Having translated the measurements of B_1, B_2, and B_3 into components B_X, B_Y and B_Z at coordinate X, Y and Z and corrected the data for the individual offsets of each Hall probe, by subtracting the measurements in zero magnetic field, it is necessary to keep track of which sensor and data set provides each measurement, since imperfections in the measurements

remain that arise from misalignment in the position and angle of the Hall probes, sensor plates and panels, and even in the motion of the chassis. The behaviour of the three components of the magnetic field for the uncorrected data is shown, plotted on different scales, in figure 6 as a function of Z, relative to the centre of MNP33, to indicate the scale and symmetry of the field in the central X–Y region of the magnet. A spread of ∼1.5 mT, measured by different Hall-probes at the same place, is most evident in the small component B_X.

By design, the three axes of each Hall probe are mutually perpendicular, with the cube onto which they are glued aligned parallel to the axes of the sensor card on which it is mounted. The sensor cards are mounted in a regular array flush onto the panels, which are aligned perpendicular to their direction of motion along the chassis, surveyed to be closely parallel to the Z axis. Any small deviation from strict parallelism, however, will mix the different field components. Referring to figure 6 to give some feeling for the importance of this mixing, we note that B_X is small in magnitude and typically $<10^{-2}$ T everywhere, B_Y is approximately 0.4 T over the central region of the magnet, while B_Z varies between 0 and 0.1 T. Then, a 1 mrad misalignment of a Hall probe will produce mixing of B_Y into B_X of $\sim 4 \times 10^{-4}$ T and of B_Z into B_X or B_Y of $\sim 10^{-4}$ T; the mixing of B_X into B_Y can be ignored. This suggests that the alignment of the Hall probes relative to the NA62 axes must be determined with a precision of <0.5 mrad to control systematic uncertainties on the field components. A second source of systematic error will arise if the locations of the Hall probes differ from their nominal positions, and this will be significant if the field gradient is large, through the relationship: $\Delta \boldsymbol{B} = \frac{\partial \boldsymbol{B}}{\partial x}\Delta x + \frac{\partial \boldsymbol{B}}{\partial y}\Delta y + \frac{\partial \boldsymbol{B}}{\partial z}\Delta z$, where $\mathbf{B}$ is the vector magnetic field. The largest field gradient is $\partial B_y/\partial y = 6 \times 10^{-4}$ T mm^{-1} at $Z = 0$ for $|Y| > 1$ m, indicating that the locations of the Hall probes must be determined to <0.5 mm. Corrections to the spatial positions of the Hall probes have been made to take into account the size of the cube on which they are mounted.

4.1. Principles for determining the angular misalignment of the Hall probes

The orientations of the 60 sets of Hall probes relative to the NA62 coordinate system consist of:

- The three angles of each Hall probe relative to the sensor-card coordinate axes, defined as α_j, β_j and γ_j, where subscripts $j = 1$, 2 and 3 refer to the particular Hall probe.
- The three angles of the sensor-card axes relative to the front or back sensor panels: $\phi_{\rm S}$, $\theta_{\rm S}$ and $\psi_{\rm S}$, respectively;
- The three angles of each of the two panels relative to the NA62 coordinate system: $\phi_{\rm P}$, $\theta_{\rm P}$ and $\psi_{\rm P}$, respectively.

All angles are small (a few mrad) and small-angle approximations are therefore valid throughout. Whilst only combinations of these different angles can be measured, it is nonetheless instructive to differentiate between the three contributions when interpreting the angular measurements, since the sensor-card and panel angles will affect the mixing of the field components differently according to the orientation of the sensor panels. Moreover, installation problems with a few of the sensor-cards that resulted in relatively large angles of ∼30 mrad can then be simply disentangled.

For the upstream data in the 'up' configuration, a little algebra gives the following two equations for the X and Y magnetic-field components:

$$B_X{}^{\rm T} = B_X{}^{\rm M} + (\beta_2 + \phi_{\rm S} + \phi_{\rm P})\, B_Y{}^{\rm M} + (\gamma_2 + \theta_{\rm S} + \theta_{\rm P})\, B_Z{}^{\rm M}, \qquad (1)$$

$$B_Y{}^{\mathrm{T}} = B_Y{}^{\mathrm{M}} + (\gamma_3 + \psi_{\mathrm{S}} + \psi_{\mathrm{P}}) B_Z{}^{\mathrm{M}}, \tag{2}$$

where $B_X{}^{\mathrm{T}}$ and $B_Y{}^{\mathrm{T}}$ are the 'true' magnetic-field components that must be determined from the measured components $B_X{}^{\mathrm{M}}$, $B_Y{}^{\mathrm{M}}$ and $B_Z{}^{\mathrm{M}}$. When the panels are rotated through $\pm 90^\circ$ to enable measurement of the components within the central region of the magnet aperture, $-360 \leqslant Y \leqslant +360$ mm, the Hall probes used to measure the X and Y components are interchanged with respect to the 'up' data. Subtly different equations then relate the mixing of magnetic-field components to the angles of the Hall probes, sensor cards, and sensor panels, as follows:

$$B_X{}^{\mathrm{T}} = B_X{}^{\mathrm{M}} + (\beta_3 + \phi_{\mathrm{S}} + \phi_{\mathrm{P}})\, B_Y{}^{\mathrm{M}} + (\gamma_3 + \psi_{\mathrm{S}} + \psi_{\mathrm{P}})\, B_Z{}^{\mathrm{M}}, \tag{3}$$

$$B_Y{}^{\mathrm{T}} = B_Y{}^{\mathrm{M}} + (\gamma_2 + \theta_{\mathrm{S}} + \theta_{\mathrm{P}})\, B_Z{}^{\mathrm{M}}. \tag{4}$$

The structure of equations (3) and (4) describing the 'Rot ± 90' data is similar to equations (1) and (2) for the 'up' data, but there are subtle differences. The mixing of B_Y into B_X introduces a new Hall-probe angle, β_3, while the angles describing the mixing of B_Z into B_X and B_Z into B_Y are interchanged between the 'up' and 'Rot ± 90' data. With suitable sign modifications to account for the rotation of the sensor panels about the Z or Y axes, equations (1)–(4) describe the field mixing for all the 'up-down' and 'Rot ± 90' data sets in both upstream and downstream data sets.

From the relative sizes of the magnetic-field components discussed in section 4 it is clear that B_X is sensitive to mixing from both B_Y and B_Z, while B_Y is rather insensitive to mixing from B_Z. Moreover, since B_Z (X, Y, Z) $= -B_Z$ (X, Y, $-Z$) for a dipole field, then B_Z (X, Y, 0) $= 0$. This suggests that an analysis of measurements of $B_X{}^{\mathrm{M}}$ in the $Z = 0$ plane will best enable the determination of $(\beta + \phi_{\mathrm{S}} + \phi_{\mathrm{P}})$, while further analysis of measurements of $B_X{}^{\mathrm{M}}$ as a function of Z will enable the determination of $(\gamma + \theta_{\mathrm{S}} + \theta_{\mathrm{P}})$, where β_2 and γ_2 refer to 'up/down' data and β_3 and γ_3 refer to 'Rot ± 90' data. Once these angular terms from equations (1) and (3) have been measured for each of the 60 sets of three sensors for all sets of data (up, down, Rot $+90$, and Rot -90 for both upstream and downstream data), corrections to B_Y can be applied directly via equations (2) and (4) using the measured values of $(\gamma + \theta_{\mathrm{S}} + \theta_{\mathrm{P}})$.

4.2. Determination of $(\beta^{\mathrm{HP}} + \phi_S + \phi_P)$ for all Hall-probe sensors

The method is straightforward in principle, namely to obtain the best estimates of the true magnetic field at (X, Y, 0) for all Hall probes (HP) in a reference data set and then by substitution in equations (1) and (3), as appropriate, obtain the combined angle at each separate value of (X, Y, 0) as:

$$\beta + \varphi_{\mathrm{S}} + \varphi_{\mathrm{P}} = (B_X^{\mathrm{T}} - B_X^{\mathrm{M}})/B^Y. \tag{5}$$

We choose a reference data set close to $X = Y = 0$ so that B_X is small and B_Y uniform and where for each sensor in the upstream data set at a given X coordinate, the same sensor in the downstream data is located at $-X$; this enables us to make use of the symmetry relation: $B_X{}^{\mathrm{T}}$ (X, Y, Z) $= -B_X{}^{\mathrm{T}}$ ($-X$, Y, Z). Extrapolating the measured values of B_X in the overlap region of both upstream and downstream data by a few mm to $Z = 0$ for all 30 sensors on each of the two sensor panels gives 30 sets of four measurements at each (X, Y, 0) position, one on the front and back sensor plane for both upstream and downstream data. Taking the average of the four values at a particular value of (X, Y, 0) with explicit notation for the particular panel and data stream, we obtain:

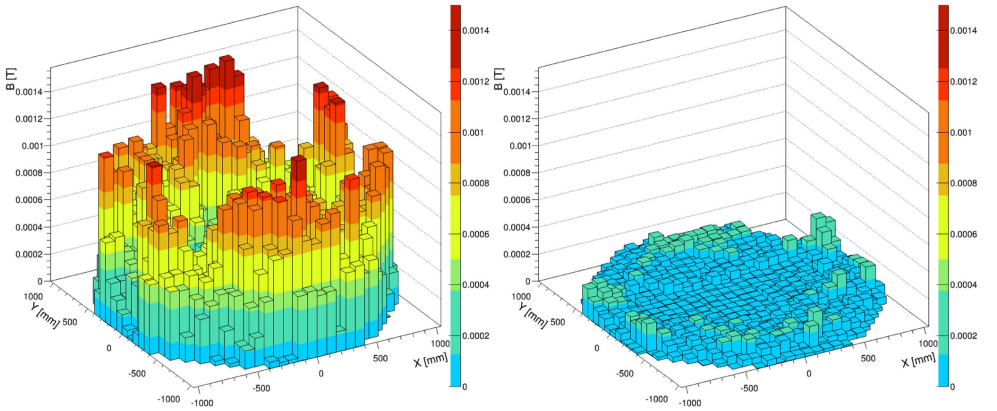

Figure 7. Residual values of B_X over the X–Y plane at $Z = 0$, (left) before corrections for Hall-probe, sensor and panel angles have been applied, (right) after applying all angular corrections.

$$B_X{}^{\mathrm{T}}(X,\,Y,\,0) = B_X{}^{\mathrm{AV}}(X,\,Y,\,0) + 1/4[((\beta^{\mathrm{HP}} + \varphi_{\mathrm{S}})_j{}^{\mathrm{U,F}} + (\beta^{\mathrm{HP}} + \varphi_{\mathrm{S}})_k{}^{\mathrm{U,B}} - (\beta^{\mathrm{HP}} + \varphi_{\mathrm{S}})_m{}^{\mathrm{D,F}} - (\beta^{\mathrm{HP}} + \varphi_{\mathrm{S}})_n{}^{\mathrm{D,B}}) + (\varphi_{\mathrm{P}}{}^{\mathrm{U,F}} + \varphi_{\mathrm{P}}{}^{\mathrm{U,B}} - \varphi_{\mathrm{P}}{}^{\mathrm{D,F}} - \varphi_{\mathrm{P}}{}^{\mathrm{D,B}})B_Y(X,\,Y,\,0), \tag{6}$$

where we have explicitly used $\beta^{\mathrm{U}} = -\beta^{\mathrm{D}}$ and $\phi^{\mathrm{U}} = -\phi^{\mathrm{D}}$ throughout. The front and back panels are labelled as F and B, respectively, and the four different sensors cards with three-component Hall probes are labelled *j, k, m* and *n*, while $B_X{}^{\mathrm{AV}}$ is the average of the four measured values of B_X.

With our choice of reference data set, the grand average over all 30 sensors on each sensor panel for the upstream and downstream data—a total of 120 measurements—gives a precise measurement of the sensor-panel angles:

$$\langle B_X{}^{\mathrm{AV}}(X,\,Y,\,0)/B_Y(X,\,Y,\,0)\rangle = -¼(\phi_{\mathrm{P}}{}^{\mathrm{U,F}} + \phi_{\mathrm{P}}{}^{\mathrm{U,B}} - \phi_{\mathrm{P}}{}^{\mathrm{D,F}} - \phi_{\mathrm{P}}{}^{\mathrm{D,B}}). \tag{7}$$

This follows from the symmetry condition $B_X{}^{\mathrm{T}}(X,\,Y,\,0) = -B_X{}^{\mathrm{T}}(-X,\,Y,\,0)$, which ensures cancellation of all 'true' magnetic fields, while the fact that for every sensor at location X in the upstream data the same sensor is at location $-X$ in the downstream data gives cancellation of the $(\beta^{\mathrm{HP}} + \phi_{\mathrm{S}})$ terms.

The values of β and ϕ_{S} for each Hall probe and sensor card are typically ∼1 mrad, whereas the panel angles, ϕ_{P}, are typically ∼10 mrad. Hence, to a very good approximation, which can be verified *a posteriori*, the four β-terms in equation (6) sum to zero. (Badly misaligned sensors at location $(X,\,Y,\,0)$ and their 'mirror-images' at $(-X,\,Y,\,0)$ were removed from the analysis, thus averaging over three, rather than four, measurements.) The best estimate of the true magnetic field $B_X{}^{\mathrm{T}}(X,\,Y,\,0)$ at each of the 30 locations in the reference data set is now given from equations (6) and (7) as:

$$B_X{}^{\mathrm{T}}(X,\,Y,\,0) = B_X{}^{\mathrm{Av}}(X,\,Y,\,0) - \langle B_X{}^{\mathrm{AV}}(X,\,Y,\,0)/B_Y(X,\,Y,\,0)\rangle B_Y(X,\,Y,\,0). \tag{8}$$

The β-terms of equations (1) and (3) are now obtained for each of the 60 sensors in the 4 reference data sets (up, down, Rot +90 and Rot −90) by substitution into equation (5).

All the Hall-probe and sensor mixing-angles are now fully determined, but only the sensor-panel angle for the reference data set. It is therefore necessary to measure the angular difference $\Delta\phi_{\mathrm{P}}$ between the panel angles for the reference data set and the data set under study

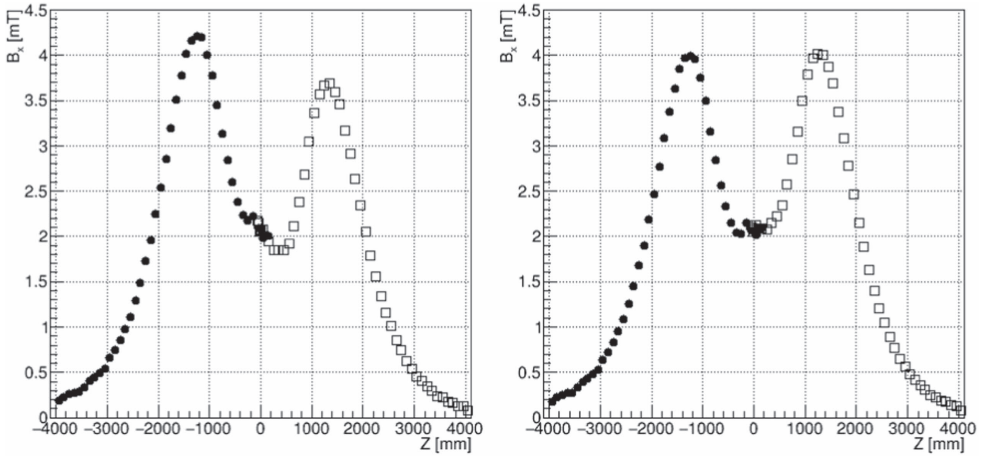

Figure 8. Variation of B_X with Z at $X = -360$, $Y = 360$ mm (left) before γ correction; (right) after γ correction. The downstream data is for sensor 27 and the upstream for sensor 10.

once the sensor and Hall-probe angles have been applied. This is possible because there are several sets of four measurements of B_X at each X–Y location. The best estimate for B_X (X, Y, 0) is then obtained as the average of all the measurements, corrected for mixing using equations (1) or (3), and the rms residual calculated. For those data sets where measurements of B_X occur at the same X, Y locations as for the reference data sets, the panel angles are varied to produce the minimum residuals. With these panel angles fixed, the residuals are examined for the data sets overlapping with the ones for which the panel angles have just been determined and the angles of the overlapping panels varied to give minimum residuals until all panel angles are fixed. The resulting residual distributions are shown in figure 7 (right), with typical residuals of $<2 \times 10^{-4}$ T to be compared with the much larger residuals prior to the angular mixing corrections, shown in figure 7 (left).

4.3. Determination of $(\gamma_2 + \theta_S)$ and $(\gamma_3 + \psi_S)$ for all Hall-probe sensors

Now that the β corrections have been made, we may subsume them into the measured values of B_X at $Z = 0$ and use simplified forms of equations (1) and (3):

$$B_X{}^{\mathrm{T}}(X, Y, Z) = B_X{}^{\mathrm{M}}(X, Y, Z) + \gamma B_Z{}^{\mathrm{M}}(X, Y, Z), \tag{9}$$

where $\gamma = (\gamma_2 + \theta_{\mathrm{S}} + \theta_{\mathrm{P}})$ or $(\gamma_3 + \psi_{\mathrm{S}} + \psi_{\mathrm{P}})$ as appropriate.

From the symmetry relationship $B_X(X, Y, Z) = B_X(X, Y, -Z)$ (see figure 6) it is apparent that $B_X{}^{\mathrm{T}}$ is symmetrical about $Z = 0$ with a local maximum or minimum. Using upstream and downstream data we therefore varied γ until this symmetry condition was achieved, as shown in figure 8. This was done for all 60 sensors separately for up, down, Rot +90, and Rot −90 data.

There are two subtleties involved in the procedure. The first is that the method is insensitive to the panel angle, θ_{P} or ψ_{P}, because of cancellation due to the panel rotation between upstream and downstream data. The second is that different sensors share the common (X, Y) coordinates for the upstream and downstream data. The method therefore involved varying two different values of γ in order to obtain the symmetrical distribution shown in figure 8. On comparing the 4 different measurements of each γ using the different

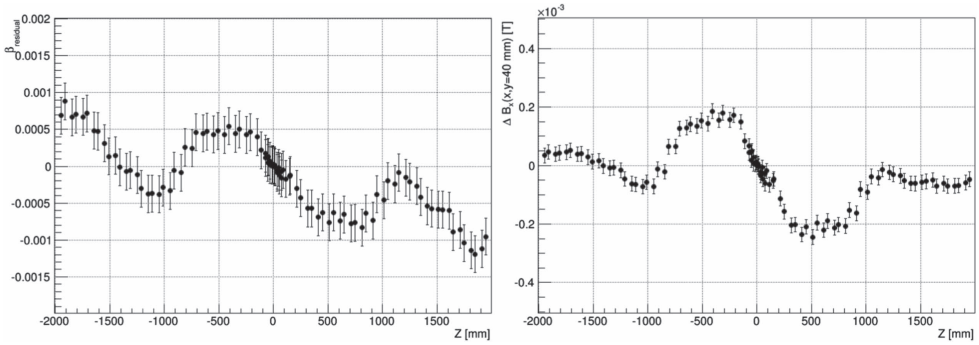

Figure 9. (Left) residual value of $\beta(Z)$ versus Z; (right) perturbation to B_X due to the residual value of $\beta(Z)$.

data sets we found agreement within ± 2 mrad for all sensors. This indicated that the panel angles θ_{P} and ψ_{P} were consistent with zero and enabled us to determine the average value of γ to within ± 1 mrad for each sensor, corresponding to a systematic uncertainty in B_X of $<10^{-4}$ T.

Using the values of γ determined from the mixing of B_Z into B_X, the measured values of B_Y were then corrected for mixing using equations (2) and (4). The consistency among the different measurements at the same values of X, Y and Z is improved, but rather less than for B_X because the mixing of B_Z into B_Y is much smaller than that of B_Y into B_X. Nonetheless the fluctuations are typically less than 5×10^{-4} T.

4.4. Variation of angle β with Z

The angular corrections for β and γ are implicitly independent of the Z coordinate of the Hall-probe sensor, but after they had been applied to all data a residual variation in β of magnitude ± 0.5 mrad was observed. The residual value, defined as the difference between the value of β (radians) at position Z and that at $Z = 0$, is plotted in figure 9 (left) for all sensors over the range -2 m $< Z < +2$ m.

Since all 60 sensors show identical behaviour this indicates that the variation in angle is due to the movement of the entire frame comprising both sensor panels. If this were caused by a small twist in the measurement chassis over its 4 m extent, then we would expect to see equal and opposite angular variations for the upstream and downstream data, since $\beta_{\mathrm{D}} = -\beta_{\mathrm{U}}$, and this is just what is seen in figure 9 (left). The angular variations of typically ± 0.5 mrad introduced by this twist are equivalent to changes in the positions of the sensors by ± 0.2 mm, which is within the variations in positions of the sensor panels recorded by the survey. The perturbation to B_X caused by this twist, which is then corrected by this analysis, is shown in figure 9 (right) and is approximately $\pm 2 \times 10^{-4}$ T over the central region of the magnet, falling off rapidly at higher values of $|Z|$ as B_Y decreases.

4.5. Magnetic-field map for the MNP33 dipole magnet

The magnetic-field map for the regular grid of measured coordinates is now obtained by taking the average value of each corrected component measured at the same value of X, Y and Z, with a statistical uncertainty on each value of B_X, B_Y and B_Z calculated as the rms deviation of the different measurements. The data is well behaved and shows the smooth variation and symmetry properties expected from a dipole field. For B_X the symmetry is perfect, but a small

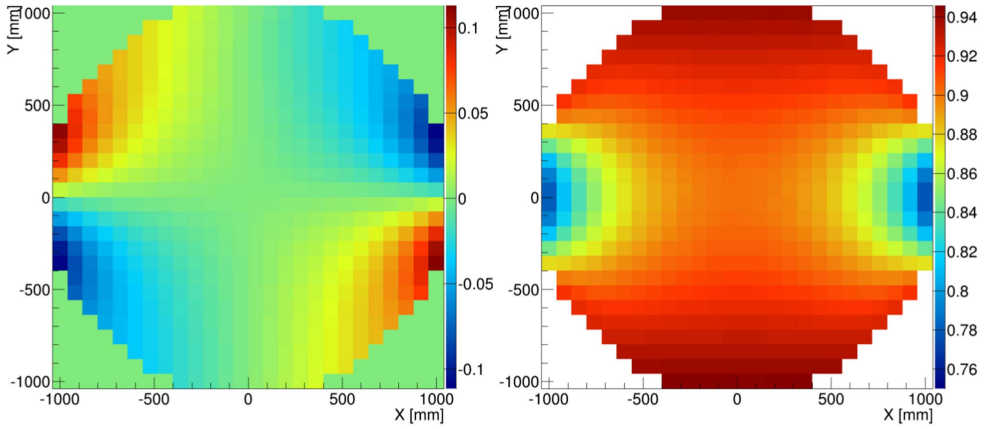

Figure 10. Integral magnetic field along the Z direction (left) $\int B_X \, \mathrm{d}Z$; (right) $\int B_Y \, \mathrm{d}Z$. The integrated X-component (left) rises to 0.1 T m for $X > 500$ mm, $Y < -500$ mm, and also for $X < -500$ mm and $Y > 500$ mm, while falling to -0.1 T m for $X > 500$ mm, $Y > 500$ mm, and also for $X < -500$ mm and $Y < -500$ mm. The integrated Y-component rises from 0.90 T m in the centre to 0.94 T m at $Y = \pm 1000$ mm, and falls to 0.76 T m for $X = \pm 1000$ mm.

asymmetry is present in the variation of B_Y with both X and Y, rising to 2×10^{-3} T at the edges of the magnet at values of $|X|$ and $|Y| = 1$ m. Magnet experts within the NA62 collaboration suggest that such an effect could easily arise during the installation and settling under gravity of the magnet coils, and we record this asymmetry as an empirical fact.

Since the secondary charged tracks make only a small angle with the beam axis, the integrated magnetic field components, $\int B_X \, \mathrm{d}Z$ and $\int B_Y \, \mathrm{d}Z$, shown in figure 10 give a good measure of how the bending power of the magnet varies across its aperture. In the central region of the magnet $\int B_X \, \mathrm{d}Z$ is zero to a good approximation, so that charged particles passing through this region are largely undeflected in the Y direction; by contrast the integrated field at values of X or Y greater than 500 mm is significant and varies strongly, with $\int B_X \, \mathrm{d}Z$ reaching ± 0.1 T m as $|X|$ approaches 1000 mm, and particles passing through these regions will experience significant deflections in the Y direction. In the central region of the magnet $\int B_Y \, \mathrm{d}Z$ is rather constant with a value of 0.90 T m, rising to 0.94 T m at $Y = \pm 1000$ mm and falling to 0.76 T m at $X = \pm 1000$ mm.

Just as for the residual magnetic field in the evacuated tubes (section 3.1), it is necessary to interpolate between the measured values on the grid, although care is needed because B_Y for the dipole magnet and its fringe field are very much larger than in the K^+ decay region. In the X–Y plane the field components have been measured on a regular square grid of side-length 80 mm, while in Z the spacing between measured grid points varies but is nowhere larger than 80 mm. Since B_X is everywhere small, linear interpolation between the grid points is adequate in X, Y and Z. Linear interpolation in X is also acceptable for B_Y since there is little variation with X. The variation of B_Y with Y is rather larger and a spline fit, with parameters determined from the three grid points on each side of the interpolation region, was initially used. A similar spline fit was also used to interpolate $\mathrm{B_Y}$ between grid points in Z. Subsequent tests, however, indicated no significant difference in any sensitive kinematic variable between using spline fits and simple linear interpolation. Since the linear interpolation is very much faster, this has been incorporated into the analysis procedure. A comparison of the field integral for B_X and B_Y at interpolated grid points in X and Y with that at neighbouring grid

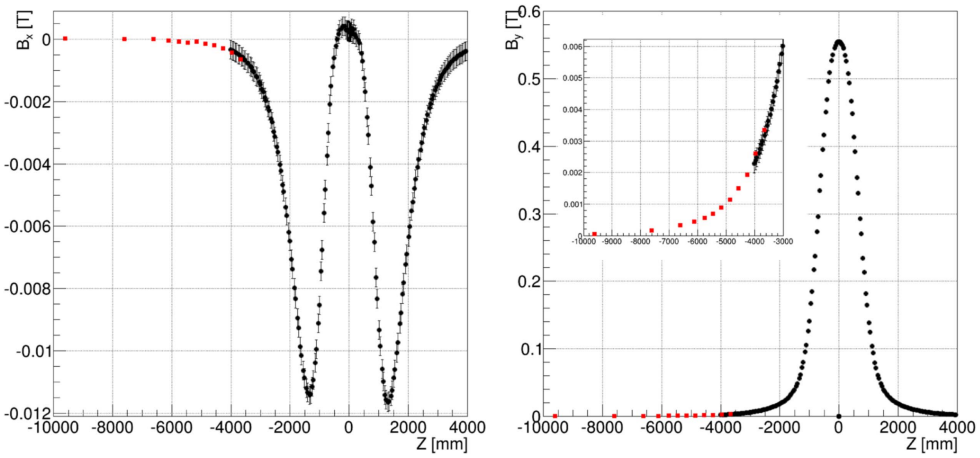

Figure 11. A comparison of (left) B_X versus Z and (right) B_Y versus Z. The majority of (black) points were measured using the MNP33 setup, while a small number of (red) points were measured with the ultra-precise setup used for the evacuated tubes.

points determined directly from the field map shows agreement everywhere to be better than 10^{-4} T m, corresponding to a fractional systematic uncertainty of less than 10^{-4} in the field integral of the major component; this is ten times less than the precision required on the field integral and confirms that systematic errors associated with interpolation are insignificant.

4.6. Systematic uncertainties on B_X, B_Y and $\int B.dL$

The following systematic uncertainties affect the magnetic-field components:

- The overall calibration of the Hall probes is good to 2×10^{-4} T at a field of 1 T and scales with the magnitude of the magnetic field. This gives a systematic uncertainty on B_Y of $\sim 10^{-4}$ T over the central region [$|Z| < 1$ m] of the magnetic field.
- There is a mismatch between upstream and downstream measurements, $\Delta B_Y{}^{\mathrm{Meas}} = (B_Y{}^{\mathrm{U}} - B_Y{}^{\mathrm{D}})$ at $Z = 0$, which is typically $<2 \times 10^{-4}$ T. This cannot arise from mixing of the B_Z component, which is zero at $Z = 0$, and therefore gives rise to a systematic uncertainty on B_Y of $\pm 10^{-4}$ T in the central region of the magnetic field.
- Measurements of β are everywhere good to ± 0.25 mrad, corresponding to ΔB_X of 10^{-4} T. Since the adjustments from data set to data set are correlated, this corresponds to a systematic uncertainty on B_X of 10^{-4} T for all measurements.
- Measurements of γ are everywhere good to ± 1 mrad, and this corresponds to ΔB_X and ΔB_Y of $\sim 10^{-4}$ T in the region around $Z = \pm 800$ mm.

All the above systematic uncertainties are uncorrelated and may be added in quadrature to give an overall systematic uncertainty on both B_X and B_Y of $\pm 2 \times 10^{-4}$ T in the central region of the magnet.

The programme of measurements of the magnetic-field components in the evacuated tubes was designed to give high-precision measurements in the fringe-field region of the dipole magnet so that a comparison could be made of the two measurements and hence an estimate be made of the systematic errors in the MNP33 magnetic-field components at large $|Z|$. In figure 11 we show the behaviour of B_X and B_Y as a function of Z for the two sets of measurements at values of $X = 500$ mm and $Y = 800$ mm, some distance from the central

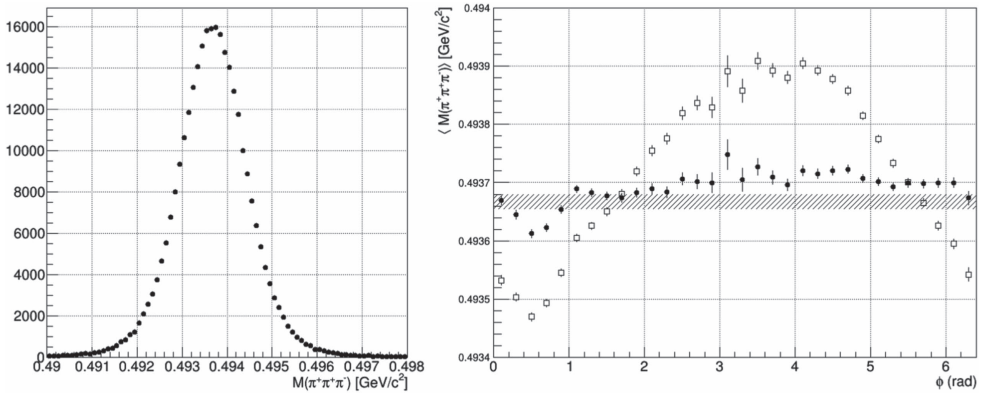

Figure 12. Left: invariant mass, $M(\pi^+\ \pi^+\ \pi^-)$, of the three charged pions in the decay $K^+ \rightarrow \pi^+\ \pi^+\ \pi^-$; right: the dependence on azimuthal angle of $M(\pi^+\ \pi^+\ \pi^-)$. The solid points are the result of applying the three-dimensional field maps obtained for both MNP33 and the evacuated tubes, whereas the open points result from applying the three-dimensional field map for MNP33 but not that for the evacuated tubes.

region of the magnet. The agreement is well within the error bars of $\pm 2 \times 10^{-4}$ T with which the MNP33 data are plotted, and we take an error of $\pm 10^{-4}$ T to be representative of all regions outside the central region of the magnet.

The statistical uncertainties at each position contribute practically nothing to the uncertainty in $\int \mathbf{B}.d\mathbf{L}$, since there are approximately 100 such uncorrelated measurements along a particle track. Our best estimates of $\Delta \int \mathbf{B}.d\mathbf{L}$ for the MNP33 dipole magnet are then: $\Delta \int B_X\ dZ = \Delta \int B_Y\ dZ = 10^{-3}$ T m. For completion, this should be added in quadrature to the systematic uncertainty of $<2 \times 10^{-4}$ T m, which was estimated for the K^+ decay region in the 90 m length of evacuated tubes.

Our analysis indicates that we have mapped the magnet fields of the NA62 experiment with a fractional, systematic uncertainty on the field integral at the level of one part in a thousand.

5. Validation of the field map using data

Whilst the small systematic uncertainty on the field integrals is a necessary condition for meeting the physics requirement that ΔP_T be determined to better than one part in a thousand, in order to preserve the precision on the angles of a particle measured by the tracking chambers in both the vertical and horizontal planes, it is not sufficient. In particular, there may still be systematic distortions in the magnetic field over the *X*–*Y* plane which would affect kinematic quantities while integrating to zero along the beam direction. Furthermore, secondary particles arising from kaons decaying at different positions along the 90 m decay region will traverse different parts of the dipole magnet and may suffer different distortions in the magnetic field. In both cases the effect will be to shift the measured momentum of a track from its true value and statistically this leads to an overall broadening of kinematic distributions. The first sensitive kinematic check is the central value and width of the invariant mass, $M(\pi^+\ \pi^+\ \pi^-)$, of the three charged pions in the decay $K^+ \rightarrow \pi^+\ \pi^+\ \pi^-$, where the momenta of the charged tracks and the vertex position were calculated from measurements made by the straw chambers. As shown on the left side of figure 12, this has a Gaussian shape

with an rms mass resolution of 720 keV$/c^2$, in excellent agreement with expectation from Monte Carlo simulation of the detector, and shows no measurable variation with the z coordinate of the kaon decay. Without the detailed corrections to the three-dimensional field map of MNP33 the resolution would be approximately twice as bad. As further confirmation of the global accuracy of the field map, the mean value of the kaon mass was found to differ from the PDG value by only two parts in 10^4, and this small effect is corrected in physics analyses by scaling all values of the magnetic-field.

Detailed studies within both the NA48 and NA62 collaborations have shown that the variation of $M(\pi^+\,\pi^+\,\pi^-)$ with the azimuthal angle around the reconstructed kaon direction is a sensitive measure of any spatial distortions of the magnetic field. On the right of figure 12 the solid points show the variation of $M(\pi^+\,\pi^+\,\pi^-)$ with azimuthal angle when the three-dimensional field maps for both the MNP33 dipole and the evacuated tubes are used, to be compared with the PDG value for the kaon mass shown as the hatched band. The angular variation of the kaon mass has an rms value of ± 30 keV$/c^2$, significantly less than one part in 10^4, and clearly indicates that no such distortions of any physical significance are present. This rms variation corresponds to a systematic uncertainty in the integrated, major component of the magnetic field of two parts in ten thousand, in confirmation of the analysis of systematic errors presented in section 4.6. While local non-uniformities in the magnetic field could, in principle, create tails in kinematic distributions they would need to be far larger than the uncertainty of $\sim 10^{-4}$ T with which the field is known at all measured grid points, and the local region would have to spread over much larger distances than the inter-grid spacing of 80 mm. Our analysis has excluded the tails arising from such local effects at the 10^{-4} level, which is sufficient for all NA62 physics.

The effect of using the three-dimensional field map for MNP33, but not making the correction for the tiny magnetic field in the evacuated tubes is shown by the open points in figure 12 (right), with a significantly increased rms of ± 150 keV$/c^2$. Given the smallness of both the individual values of magnetic field and their integral values, this result shows that the painstaking effort to measure with exceptionally high precision the residual magnetic field in the evacuated tubes (section 2.1) was essential. Although it would make little sense to analyse the high-precision data of NA62 using a simple $p_{\rm T}$ kick of 270 MeV$/c$ in place of the three-dimensional dipole field map, we note in passing that the effect of doing so would be to broaden the three-pion mass resolution by a factor of two and introduce an azimuthal variation of several MeV$/c^2$.

It is important to note that the results presented here arise from a convolution of the systematic errors in the magnetic field map and those arising from any misalignment of the straw tubes. As such, the systematic uncertainties attributed to the magnetic field are, if anything, over-estimated and the level of validation is therefore completely robust. One can also judge that any misalignment of the straw tubes can only be very minor and have no measurable consequences for the physics. The effect of the systematic uncertainties in the magnetic-field map are much smaller than those arising from the measurements in the GTK and straw detectors, as we discuss in section 1, and we therefore conclude that the measurements and analysis of the combined magnetic fields in MNP33 and the evacuated tubes have been performed satisfactorily.

6. Summary

We have explained the reasons for making a precise determination of the three-dimensional magnetic field maps of both the dipole magnet MNP33 and the evacuated tubes, and have

described in some detail both the measurement procedures and the analysis by which the raw measurements of the magnetic field were corrected to eliminate systematic measurement errors. It is worth noting that the high-precision measurements detailed in this paper were made over a volume of more than 600 m^3. The physics requirements were specified to be that ΔP_T be determined to better than one part in a thousand, corresponding to $\Delta \int \mathbf{B}.d\mathbf{L} < 10^{-3}$ T m. Our analysis in section 4.6 has indeed shown that this accuracy in the integrated field was achieved on both the major, *Y*-component, and minor, *X*-component, of the magnetic field and equally importantly that the two integrated components of the magnetic field in the 90 m long evacuated tubes were each measured with an uncertainty of less than 2×10^{-4} T m. However, this condition on the integrated field of the major component, although necessary, is not sufficient on its own for the very precise physics analyses of NA62. Physics quantities, and in particular the variation with azimuthal angle of the invariant mass of the three charged pions, are sensitive to potential distortions of the magnetic field in the *X*–*Y* plane in addition to the integrated values, and we have shown in section 5 that this variation has been reduced to a level which is small compared with that expected from measurement uncertainties in the GTK and STRAW chambers. We have also ruled out the possibility of local non-uniformity of the magnetic field causing tails on kinematic distributions of any consequence to the physics analysis. Our conclusion is that the combined magnetic field maps of MNP33 and the evacuated tubes fully meet the physics requirements of NA62.

Acknowledgments

The authors are grateful to CERN for providing the beam and infrastructure necessary to this work and to all our colleagues within the NA62 collaboration, and especially the Straw Tracking Group, for their fulsome support and for allowing us to use the data from which figure 12 was made. We are grateful to Michael Nelson for his contribution to the measurement and analysis of the magnetic field in the NA62 evacuated tubes and to Anne Chappuis and Evgueni Goudzovski for interpolating the field measurements and providing the code for correcting the track propagation within the evacuated tubes. We thank Antonio Goncalves Martin de Oliviera for making essential fittings and fixtures and Ferdinand Hahn for organising the resources that enabled the measurements to be made. One of the authors (JRF) thanks the ERC [UniversaLepto, grant 268062] and STFC for financial support during this work.

References

[1] Brod J, Gorbahn M and Stamou E 2011 *Phys. Rev.* D **83** 034030
Buras A, Buttazzo D, Girrbach-Noe J and Knegjens R 2015 *J. High. Energy. Phys.* JHEP1511 (2015)033
[2] Anelli G *et al* 2005 Proposal to measure the rare decay $K^+ \to \pi^+ \nu \nu$ at the CERN SPS *CERN-SPSC-2005-013*
[3] Hahn F 2010 *NA62 Technical Design Document NA62-10-07* (http://na62.web.cern.ch/NA62/Documents/TDR)
[4] Goudzovski G *PhD Thesis* (http://goudzovs.web.cern.ch/goudzovs/phd-goudzovski.pdf)
[5] Griesmayer E, Neuhofer G, Bergsma F, Grillet J P, Dalpiaz P F, Duclos J and Petrucci F 1995 Comparison of field calculations and measurements of a spectrometer magnet *Nucl. Instrum. Methods Phys. Res.* A **361** 466–71
[6] Aleksa M *et al* 2008 Measurement of the ATLAS solenoid magnetic field *J. Instrum.* **3** 04003